Frontiers of Optoelectronics (2022) 15:43
https://doi.org/10.1007/s12200-022-00044-1

Frontiers of Optoelectronics

RESEARCH ARTICLE

Dark current modeling of thick perovskite X-ray detectors

Shan Zhao[1] · Xinyuan Du[1] · Jincong Pang[1] · Haodi Wu[1] · Zihao Song[1] · Zhiping Zheng[1,2] · Ling Xu[1,2] · Jiang Tang[1,2] · Guangda Niu[1,2]

Received: 14 June 2022 / Accepted: 17 July 2022

Abstract
Metal halide perovskites (MHPs) have demonstrated excellent performances in detection of X-rays and gamma-rays. Most studies focus on improving the sensitivity of single-pixel MHP detectors. However, little work pays attention to the dark current, which is crucial for the back-end circuit integration. Herein, the requirement of dark current is quantitatively evaluated as low as 10^{-9} A/cm^2 for X-ray imagers integrated on pixel circuits. Moreover, through the semiconductor device analysis and simulation, we reveal that the main current compositions of thick perovskite X-ray detectors are the thermionic-emission current (J_T) and the generation-recombination current ($J_{g\text{-}r}$). The typical observed failures of p–n junctions in thick detectors are caused by the high generation-recombination current due to the band mismatch and interface defects. This work provides a deep insight into the design of high sensitivity and low dark current perovskite X-ray detectors.

Keywords Perovskite · X-ray detection · Dark current · Semiconductor simulation · Junction device

1 Introduction

Metal halide perovskites (MHPs) have attracted extensive interest in X-ray and gamma-ray detection, due to their properties such as high atomic numbers, large mobility-lifetime ($\mu\tau$) products, defect tolerance, and low-temperature solution processability [1–4]. Many efforts have been made to improve the sensitivity of perovskite X-ray detectors, since the high sensitivity can benefit signal-to-noise ratio and reduce harmful radiation dose [5–11]. For example, the sensitivity has been rapidly increased from 80 to 23,600 μC/(Gy_{air}·cm^2) for $MAPbBr_3$ single crystals, through strategies of crystal quality enhancement and interface engineering [5, 6, 12].

However, most of these studies focus on single-pixel devices without circuit integration. To achieve flat panel X-ray imagers (FPXIs), the semiconductor detectors should be integrated on TFT or CMOS pixel circuits. This means that the device dark current is an important figure of merit to be considered. However, previous work has paid little attention to the dark current. Currently, the dark current of perovskite X-ray detectors is in the range of $10^{-8}-10^{-5}$ A/cm^2, which is 1 to 4 orders higher than that of other semiconductor X-ray detectors such as α-Se and CdZnTe [13–15]. Moreover, the design strategy of the device structure for decreasing dark current is also not clear.

Herein we quantitatively evaluate the dark current requirement according to the standard process of TFT or CMOS fabs. For FPXIs, the response of the detector is firstly stored in the collection capacitor of the pixel circuit, whose capacitance is C_{st}, and then converted to accumulated charges. When the dark current increases, the accumulated charges rise and thus reduce the dynamic response range of the imager, as shown in Fig. 1a. For pixel circuits, there is a definite threshold voltage ΔV_{max}, beyond which charges cannot be stored in the collection capacitor. According to this threshold voltage, we can derive the full well capacity (FWC) for a given pixel circuit as $FWC = C_{st} \times \Delta V_{max}$. Then we can obtain the threshold of the response current density (J_{max}), beyond which the circuit cannot differentiate the intensities of responses, as $J_{max} = (C_{st} \times \Delta V_{max})/(A \times t)$, where A is the pixel area, t is the integration time. For a typical dynamic FPXI (frame rate: 30 fps), A is 150 × 150 μm^2, t is 33 ms, C_{st} is ~ 1 pF for a 150 × 150 μm^2 pixel, and ΔV_{max} is set as 1.5 V [16]. Then J_{max} can be estimated as ~ 2×10^{-7}

✉ Guangda Niu
guangda_niu@hust.edu.cn

[1] Wuhan National Laboratory for Optoelectronics and School of Optical and Electronic Information, Huazhong University of Science and Technology, Wuhan 430074, China

[2] Optical Valley Laboratory, Wuhan 430074, China

Published online: 31 October 2022

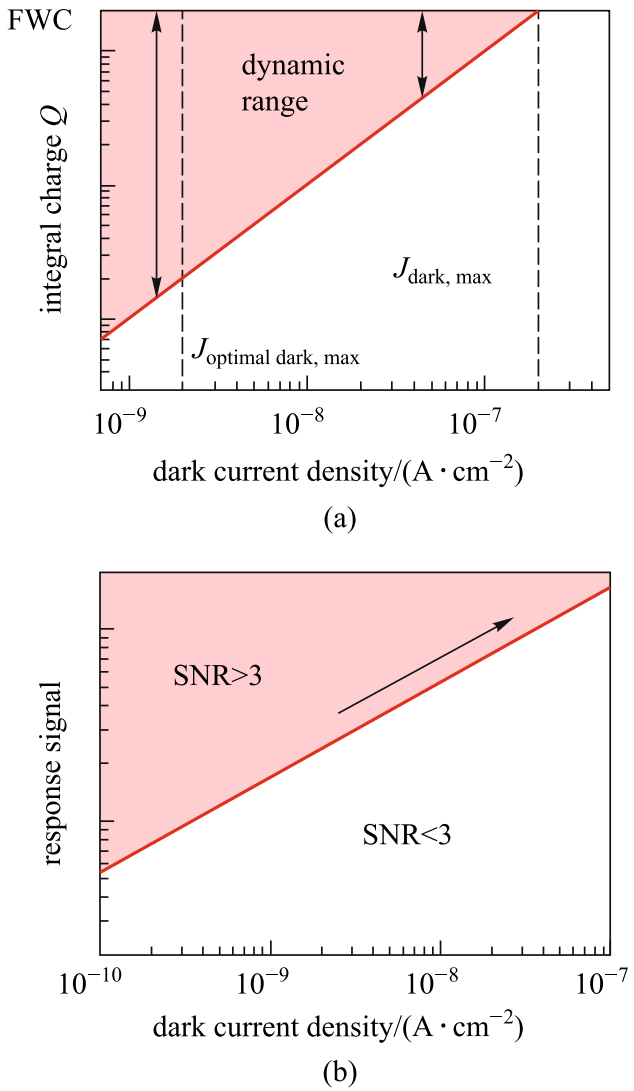

Fig. 1 Schematic illustration of the influence of dark current in FPXIs. **a** Integral charge (Q) against the dark current density J_{dark}. When J_{dark} flushes the collection capacitor to FWC within t, the dynamic range diminishes to 0. **b** Minimum detectable signal ($J_{signal, min}$) against the dark current density (J_{dark}). $J_{signal, min}$ is the response signal of the minimum detection dose, corresponding to a minimum detectable signal-to-noise ratio (SNR) of 3 [33]

A/cm^2. The dark signal should be limited to a maximum of 1% of J_{max} [17], i.e., ~ 10^{-9} A/cm^2, to guarantee the response dynamic range.

Moreover, the dark current can also cause noise fluctuations. The detector noise is mainly composed of thermal noise, shot noise, and 1/f noise [18]. The 1/f noise decays rapidly with frequency and can be eliminated by interface optimization. The thermal noise ($I_{n,t}$) and shot noise (I_n) are defined as $I_{n,t} = \sqrt{4kT\Delta f/R}$ and $I_n = \sqrt{2e\Delta f \cdot I_{dark}}$, respectively, where R is the bulk resistance of the detector, k is the Boltzmann constant, T is the temperature, I_{dark} is the dark current, and Δf is the bandwidth in the frequency domain.

For the typical photo-conducting detectors, it is clear that the dark current directly or indirectly aggravates the noise signal. The signal-to-noise ratio of the X-ray flat plate detector is increased by noise enhancement, as shown in Fig. 1b.

To decrease the dark current, the bulk resistance of perovskite semiconductors should be enhanced, which is inversely proportional to the carrier concentration and mobility. Many efforts have been devoted to decreasing the carrier concentration and approaching the intrinsic semiconducting property [7, 11, 19, 20], but only a few cases have succeeded. The study of solar cells, LEDs and photodetectors has shown that Schottky junction and p–n junction type devices are effective in suppressing the dark current [21, 23]. It should be noted that all the above-mentioned devices are based on thin films, where the thickness of the photosensitive layer is hundreds of nanometers for solar cells and photodetectors, and < 100 nm for LEDs [24]. However, for X-ray detectors, the thickness of the photosensitive layer should be hundreds of micrometers, considering the high penetration capability of X-rays [1]. For thick X-ray or gamma-ray perovskite detectors, the rectification ratios of junction devices are generally poor, especially for p–n junctions (Table 1). The underlying mechanism is still not clear.

In this work, through semiconductor device analysis and simulation, we reveal that the main current compositions of junction devices are the thermionic-emission current (J_T) and the generation-recombination current ($J_{g\text{-}r}$). The junction can effectively suppress J_T by constructing the carrier blocking barrier. The low barrier at the p- or n-layer is one reason for the poor performance of thick p–n junction detectors. In addition, non-ideal $J_{g\text{-}r}$ is another critical issue degrading the performance of devices. Both heterojunction band mismatches and traps within bulks or interfaces are the cause of $J_{g\text{-}r}$. We determine experimentally that the interfacial defects are prone to cause the failure to form a junction region between the thick perovskite layer and thin p- or n-layer. We believe that the key to obtaining excellent thick detectors is the fabrication of p–n junctions with band match and without introducing interface defects.

2 Theoretical dark current modeling of thick devices

Figures 2a, b exhibit energy band diagrams of the basic Metal-Semiconductor-Metal (MSM) device with thin and thick photosensitive layers. Theoretically, two depletion regions are formed at the two sides of the device due to the Schottky barriers between the electrode and the high-resistivity perovskite. If the photosensitive layer thickness is less than the depletion region width, as shown in Fig. 2a,

Table 1 Summary of the junction structures and rectification ratios of MHP polycrystalline thick film or bulk single crystal detection devices

Material	Perovskite morphology	Device structure	Structure type	Rectification ratio
$MAPbI_3$ [25]	Single crystal	Ga/$MAPbI_3$/Au	Schottky junction	1100 (@ ± 20 V)
$CsPbBr_3$ [26]	Single crystal	Ga/$CsPbBr_3$/Au	Schottky junction	962 (@ ± 35 V)
$CsPbBr_3$ [7]	Polycrystalline film	Au/$CsPbBr_3$/FTO	Schottky junction	21 (@ ± 1.5 V)
$CsPbBr_3$ [27]	Single crystal	EGaIn/$CsPbBr_3$/Au	Schottky junction	550 (@ ± 200 V/cm)
		Ga/$CsPbBr_3$/PTAA/Au	Schottky junction	660 (@ ± 100 V/cm)
		Ag/C_{60}/$CsPbBr_3$/PTAA/Au	p–n junction	1.0 (@ ± 110 V/cm)
$MAPbBr_3$ [12]	Single crystal	Au/$MAPbBr_3$/C_{60}/BCP/Ag	p–n junction	1.1 (@ ± 0.5 V)
$MAPbBr_3$ [28]	Polycrystalline polymer film	Cu/BCP/C_{60}/$MAPbBr_3$&PMMA/NiO_x/ITO	p–n junction	1.0 (@ ± 1.0 V)
$MAPbBr_3$ [29]	Single crystal	Cr/$MAPbBr_3$/C_{60}/BCP/Cr	p–n junction	3.3 (@ ± 5.0 V)
$MAPbBr_3$ [6]	Single crystal	Au/poly-TPD/$MAPbBr_3$/C_{60} /PCBM/Ag	p–n junction	1730 (@ ± 29 V)
$MAPbI_3$ [30]	Polycrystalline film	ITO/TiO_2/$MAPbI_3$/Spiro-MeOTAD/ITO	p–n junction	1.6 (@ ± 40 V)
$Cs_{0.15}FA_{0.85}PbI_3$ [31]	Polycrystalline filled film	C/$Cs_{0.15}FA_{0.85}PbI_3$/C_{60}/BCP/Cr	p–n junction	1.3 (@ ± 25 V)
Cs_2TeI_6 [32]	Polycrystalline film	Au/PTAA/Cs_2TeI_6/TiO_2/FTO	p–n junction	1.4 (@ ± 0.5 V)

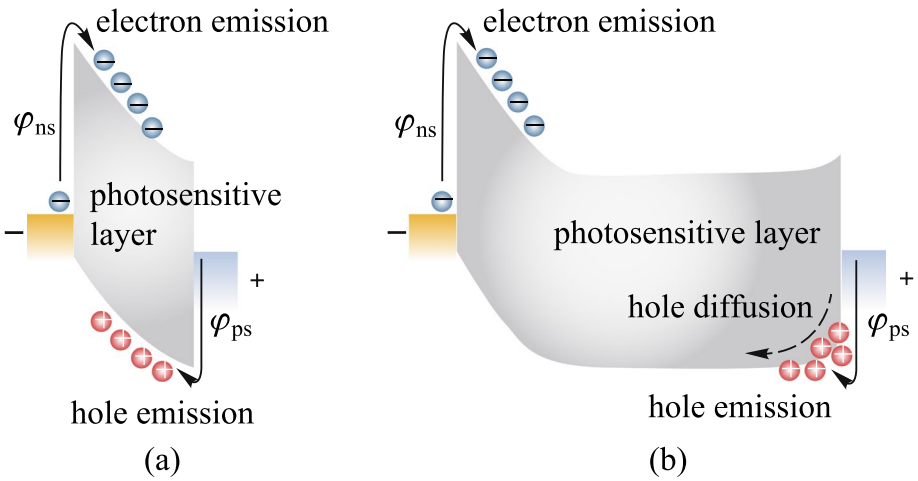

Fig. 2 Energy band diagrams of the Metal-Semiconductor-Metal (MSM) device with **a** thin and **b** thick photosensitive layers

the junction regions are punched through, which is a full depletion case [34]. The depletion region width X_d can be approximately calculated as Eq. (1) [35]

$$X_d = \left[\frac{2\varepsilon(V_D - V)}{qN_d}\right]^{1/2}, \quad (1)$$

where q is the electron charge, ε is the dielectric constant, N_d is the doping concentration of the semiconductor, V is the operating voltage, and V_D is the barrier height, i.e., $V_D = W_m - W_s$. W_m and W_s are the work function of metal electrode and the semiconductor, respectively. For MHPs, X_d is approximately 10 μm for barrier height of 1 V, where ε is $10\varepsilon_0$ and N_d is 10^{14} cm^{-3} for $MAPbI_3$ polycrystalline films [36, 37]. For thin-film detectors with thickness of hundreds of nanometers, X_d is much larger than the layer thickness L and the device is fully depleted. For thick X-ray detectors, the thick layer makes it difficult to obtain a fully depleted device. Assuming $X_d = L = 200$ μm, the punch-through voltage V_{PT} is calculated as ~ 4000 V using Eq. (1). The neutral region cannot effectively collect generated charges due to the absence of electric field [35]. Therefore, it is necessary to reduce the thickness or enhance the operating voltage to achieve full depletion and obtain a high detection efficiency.

On the other hand, theoretically, incomplete depletion would not degrade the dark performance of the junction device. For the Schottky contact where the depletion region is the barrier layer, the dark current is determined by carrier injection, following the thermionic-emission theory as represented by Eq. (2) [38]

$$J_T = A^* \cdot T^2 \cdot e^{-\frac{q\varphi_s}{kT}} \cdot \left(e^{\frac{qV}{kT}} - 1\right), \quad (2)$$

where A^* is Richardson constant, which is 120 A/(cm^2·K^2) for vacuum, $q\varphi_s$ is the barrier height of carrier injection. The reverse saturation dark current is only related to φ_s. When the carrier injection barrier is higher than 1 eV, the theoretical dark current is lower than 2×10^{-10} A/cm^2. For Ohmic-like contact where the depletion region is the accumulation layer, the current source is a synthesis of carrier thermionic-emission and diffusion process [35]. Injected carriers are accumulated in the depletion region, and this impedes the flow of carriers, which then relies on diffusion movement to enter the semiconductor interior. Correspondingly, the diffusion current J_D is lower than J_T for the same barrier. Hence as long as sufficiently high barriers are constructed on both sides of contacts, fully depleted thin- and non-fully depleted thick-film devices both can realize theoretically low dark currents. The p–n junction device can construct higher barriers than that of the Schottky junction by introducing the blocking layer (BL), thus to more effectively suppress the dark current.

The generation-recombination current ($J_{g\text{-}r}$) is another crucial source of the dark current, which is the main cause for deterioration of the J–V characteristic of the device. $J_{g\text{-}r}$ is contributed by the bulk depletion region and the interface. For the bulk layer, according to the Shockley–Read–Hall (SRH) recombination model, $J_{g\text{-}r}$ can be calculated using Eq. (3) [39]

$$J_{g\text{-}r} = \frac{qn_iX_d}{2\tau}\left(e^{\frac{qV}{2kT}} - 1\right), \tag{3}$$

where n_i is the intrinsic carrier concentration, and τ is the non-equilibrium carrier lifetime, which is inversely proportional to the trap concentration N_t. $J_{g\text{-}r}$ is proportional to N_t and X_d, and cannot be suppressed by the barrier. Since the thickness of the X-ray detectors is as large as tens to hundreds of microns, $J_{g\text{-}r}$ is significantly raised with the increase of the perovskite trap concentration.

As shown in Additional file 1: Fig. S1, the interface defects and the energy band offset of the p–n heterojunction would lower the thermionic emission barrier $q\varphi_s$, and facilitate undesired charge generation at the interface [40]. Therefore, in order to obtain high-performance thick junction devices, in addition to building a high barrier by the BL to reduce J_T, the photosensitive layer should be synthesized with few bulk and interface traps, and the BL should maximize φ_s with matched E_c or E_v to reduce $J_{g\text{-}r}$. Currently, the performance of p–n junction devices is inferior to that of a Schottky junction, which is to be expected due to the combined result of unsuitable BL (with low blocking barriers) and interfacial defects.

3 Simulation modeling and parameters

To further verify the above analysis, the X-ray detectors were simulated by Solar Cell Capacitance Simulator (SCAPS) software. $MAPbI_3$ was selected as the photosensitive layer of the detector. The material parameters are listed in Table 2. Two types of defects in the bulk layer were set, containing shallow donor and deep neutral defects. The shallow donor density was set as 1×10^{14} cm^{-3}. The deep defects were located at the most effective level as the band gap center (E_i), whose density was 10^{12} cm^{-3} [37].

Table 2 Details of basic parameters used for the simulation of $MAPbI_3$ and SnO_2 layer

Parameters	$MAPbI_3$	SnO_2
Thickness/μm	0.8/200	0.1
Band-gap/eV	1.5 [42]	3.6 [45]
Electron affinity/eV	3.9 [42]	4.0 [45]
Dielectric permittivity (relative)	30 [43]	9 [45]
CB effective density of states/cm^{-3}	2.5×10^{20} [43]	2.2×10^{18} [45]
VB effective density of states/cm^{-3}	2.5×10^{20} [43]	1.8×10^{19} [45]
Electron thermal velocity/(cm·s^{-1})	1×10^{7}	1×10^{7}
Hole thermal velocity/(cm·s^{-1})	1×10^{7}	1×10^{7}
Electron mobility/(cm^2·V^{-1}·s^{-1})	10 [44]	100 [45]
Hole mobility/(cm^2·V^{-1}·s^{-1})	10 [44]	25 [45]
Donor density/cm^{-3}	1×10^{14} [37]	1×10^{16}/0
Acceptor density/cm^{-3}	0	0/1×10^{16}
Defect type	Neutral	Neutral
Capture cross section of electrons/cm^2	1×10^{-14}	1×10^{-14}
Capture cross section of holes/cm^2	1×10^{-13}	1×10^{-14}
Defect energy level above E_i/eV	0	0
Defect density/cm^{-3}	1×10^{12} [37] (1×10^{10} – 1×10^{15})	1×10^{14}

We designed Schottky junctions with various contact electrodes and p–n junction with SnO_2 layer, respectively. The Schottky junction device was composed of ITO/$MAPbI_3$/Au or Ga, while the structure of the p–n junction device was ITO/SnO_2/$MAPbI_3$/Au or Ga. SnO_2 has been widely used as the electron transport layer in p–i–n perovskite solar cells [41]. The donor density of SnO_2 was set as 1×10^{16} cm^{-3}. The parameters of contact electrodes are listed in Table 3. The back metal was a Schottky contact electrode such as Au (5.1 eV) and Ga (4.2 eV). Gold electrodes are widely used for perovskite radiation detectors, while Ga has been studied for Schottky contact of $CsPbBr_3$ single crystal [26].

Table 3 Material parameters of the contact electrodes

Parameters	Au	ITO	Ga
Electron recombination velocity/(cm·s^{-1})	1×10^5	1×10^7	1×10^5
Hole recombination velocity/(cm·s^{-1})	1×10^7	1×10^5	1×10^7
Metal work function/eV	5.1	4.7	4.2
Allow contact tunneling	On	On	On

4 Results and discussion

As shown in Fig. 3a, the Schottky device with ITO/$MAPbI_3$/Au structure was simulated to analyze the dark current source. The bias voltage was applied to the Au electrode. The thicknesses of $MAPbI_3$ were 200 and 0.8 μm, corresponding to thick X-ray detectors and thin-film photodetectors. We set a range of deep defect concentrations N_t of the perovskite layer from 10^{10} to 10^{15} cm^{-3}, corresponding to high-quality single crystals and polycrystalline films [37]. The simulated current density–voltage (*J*–*V*) characteristic curves of the two devices with different thicknesses were obtained as shown in Fig. 3b, c. With a negative bias on the Au contact, the high electron-injection barrier of 1.2 eV could lead to a low reverse current. For the thin-film device, no difference in the *J*–*V* curves was found for various defect concentrations. The reverse currents of the thin device all were 1.7×10^{-7} A/cm^2 at − 0.7 V. This thin device was fully depleted as shown in Additional file 1: Fig. S2. The theoretical dark current density was dominated by J_T, which could be calculated by Eq. (2) as the sum of 3×10^{-14} A/cm^2 (for

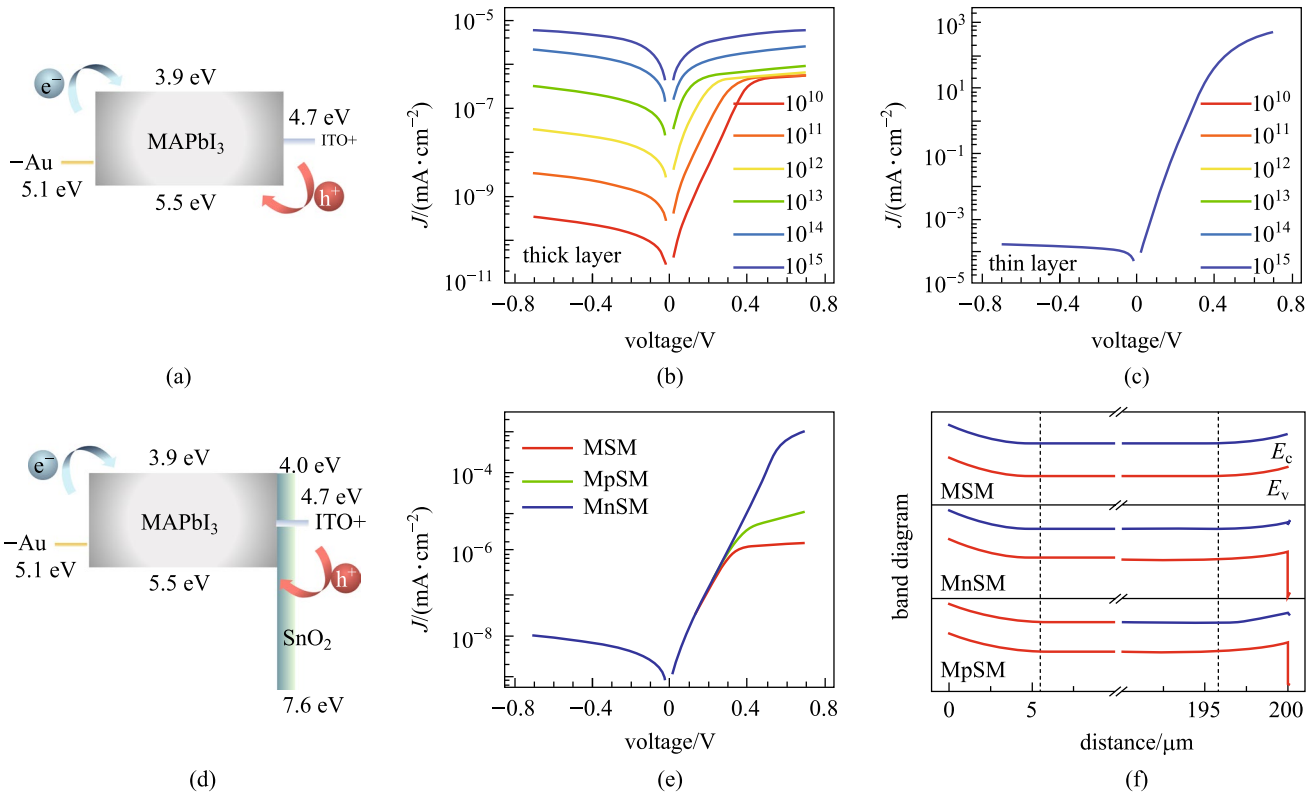

Fig. 3 Simulated structures and output performances of $MAPbI_3$ detectors. **a, d** Band diagram of $MAPbI_3$ devices with **(a)** the Schottky junction and **(d)** the p–n junction. **b**, **c** are the simulated *J*–*V* curves of thick layer and thin layer devices based on the structure (**a**), with different deep defect concentrations. **e** Comparison between the simulated *J*–*V* characteristics with Schottky, n-type and p-type junction, where M denotes Au or ITO electrode, S denotes $MAPbI_3$ semiconductor, and n or p denotes n-type or p-type SnO_2 layer. **f** Simulated energy band of devices with Schottky, n-type and p-type junction

electrons with a 1.2 eV barrier) and 1×10^{-7} A/cm^2 (for holes with a 0.8 eV barrier). The estimated J_T was consistent with the simulation results of the current for the thin-film device. In Additional file 1: Fig. S3, $J_{g\text{-}r}$ of this device was shown to have changed from 5×10^{-15} to 5×10^{-10} A/cm^2 with the increase of N_t, which could be negligible compared with J_T. For the thick device, the current rose from 3.4×10^{-13} to 6.1×10^{-9} A/cm^2 at − 0.7 V bias with the increase of N_t. Simultaneously, the rectification ratio decreased to 1 at ± 0.7 V. This was due to J_T of holes being suppressed by the accumulation region on ITO side, and $J_{g\text{-}r}$ became an important current composition. In this case, the quality of photosensitive material significantly influenced the performance of the thick junction detector.

Furthermore, we simulated the p–n junction device of perovskite X-ray detectors. Figure 3d showed the energy band of ITO/SnO_2/$MAPbI_3$/Au junction device. SnO_2 layer served as a high hole-injection barrier of 2.9 eV. In Fig. 3e, whether SnO_2 layer is n-type or p-type semiconductor, the rectifying junction was oriented in the same direction. Figure 3f can confirm that the band bending of the $MAPbI_3$ depletion region was almost unchanged whether adding SnO_2 layer or not. The widths of the depletion region were the same, which were 5.5 μm at Au contact and 4.2 μm at ITO contact. Consequently, we consider that the transport layer of p–n junction in thick devices hardly influences the depletion region and it acts as a charge blocking layer. In addition, Fig. 3e showed that the current densities for devices with Schottky, n-type and p-type junction were all 1.0×10^{-11} A/cm^2 at − 0.7 V, because SnO_2 only blocks the injection of holes which hardly contributes to the dark current. SnO_2 layer is hole-blocking by virtue of the matched conduction band and deep valence band. Its carrier type is not critical for the reverse current of the thick device.

We studied the influence of Schottky barrier for X-ray thick detectors using two metal–semiconductor contacts of Ga/$MAPbI_3$ and Au/$MAPbI_3$. The device structure with the Ga electrode was shown in Fig. 4a. The bias voltage was applied to the Ga electrode. The work function of Ga metal (as 4.2 eV) was matched with the fermi level of $MAPbI_3$ (as 4.198 eV by simulation), so the Ga electrode was an ohmic contact. Figure 4b displays the simulated energy band of this device, showing the band on the Ga side was flat and the junction region was on the SnO_2/ITO side. In Fig. 4c, since

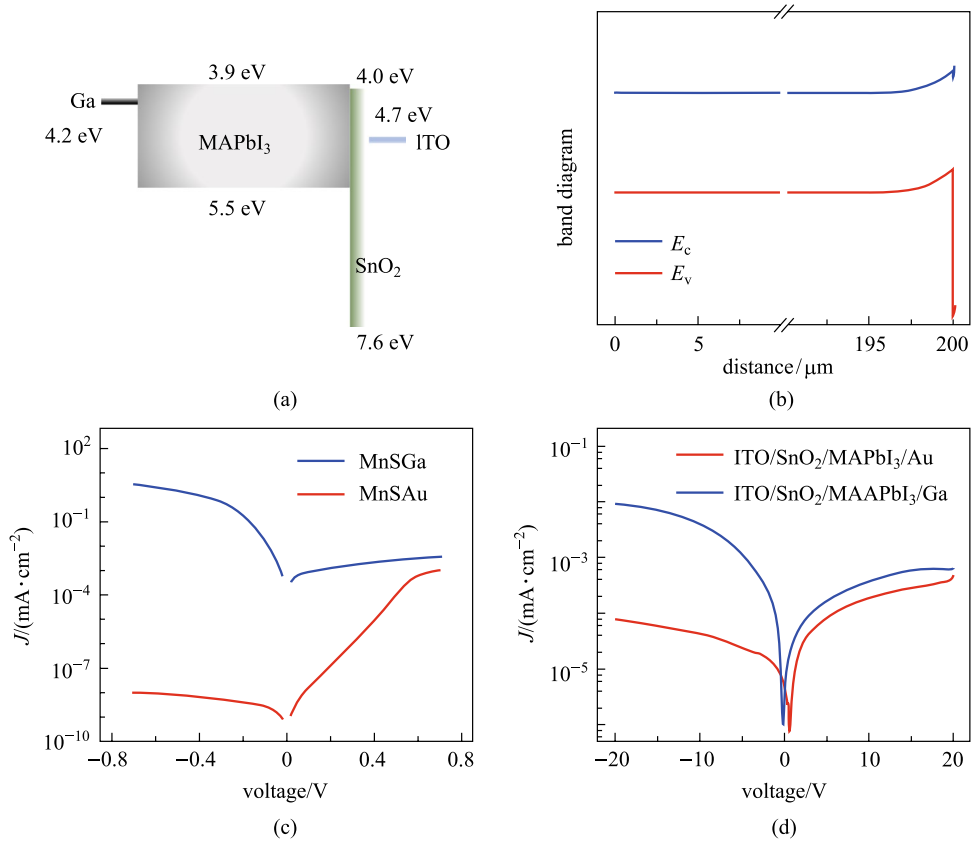

Fig. 4 Simulated and experimental characteristics of Schottky devices. **a** Band diagram of the junction device with Ga electrode. **b** Simulated energy band of the junction device with Ga electrode. Comparison of the **c** simulated and **d** experimental *J*–*V* curves with Au and Ga metal contacts

the barrier V_D of Ga electrode (0.002 eV) was much lower than that of Au electrode (0.9 eV), J for the device with Ga electrode (3.4×10^{-3} A/cm^2) was 8 orders higher than that with Au electrode at − 0.7 V bias. This effectively illustrates that the high Schottky barrier played an important role in blocking carrier flow and reducing the dark current.

Following the simulated structure as mentioned above, we fabricated the X-ray detector employing perovskite. We used the process of one-step blade-coating to fabricate $MAPbI_3$ polycrystalline thick films. This method has the advantages of easy preparation of functional layers, large area, and easy integration at low temperature, which is compatible with the processing of TFT circuits [30, 46]. A detailed description of the fabrication is provided in the supplementary Additional file 1: "Experimental Section". The J–V curves of the experimental detector are shown in Fig. 4d. Under − 20 V bias, J for the case of Ga electrode (9.2×10^{-6} A/cm^2) was higher than that of Au electrode (7.6×10^{-8} A/cm^2). The device rectification was similar to the simulation result, indicating the validity of Schottky junction in practice. In previous studies, the Schottky device structure has been applied in X-ray/gamma-ray detectors of perovskite single crystal or polycrystalline films, and has been confirmed to be beneficial for obtaining steady low dark currents [25, 27].

Although the experimental device of ITO/SnO_2/$MAPbI_3$/Au structure exhibits $J-V$ characteristic similar to the simulation result, the rectification ratio is just 5.6 at ± 20 V which is 4 orders lower than the simulated theoretical value (~ 10^5 at ± 0.7 V). In the simulation, the interface was considered to be a perfect contact and interfacial defects were ignored. However, interfacial defects were believed to be an important reason for deteriorating perovskite detectors. Here we prepared two kinds of blocking layers, one of SnO_2 and the other of NiO_x, to analyze the influence of the bottom interface of thick perovskite films. The SnO_2 layer was fabricated by spinning coating the colloidal dispersion, and NiO_x was deposited by radio frequency (RF) sputtering. The band structure of the device with NiO_x layer is shown in Additional file 1: Fig. S4a [47]. NiO_x acted as an electron blocking layer, with an electron injection barrier of 2.9 eV. Theoretically, the device with NiO_x is reverse-biased under positive voltage (where electrons are injected from ITO), while the device with SnO_2 layer is reverse-biased under negative voltage. This can be corroborated by the simulated $J-V$ curve in Additional file 1: Fig. S4b. Figure 5a shows the $J-V$ curves of the experimental devices with SnO_2 and NiO_x layer. The devices showed similar rectification characteristics, with rectification ratios of 5.6 and 4.7 at ± 20 V, respectively. The results indicated that the bottom interface of thick perovskite films did not form a junction with the blocking layer. High concentrations of interfacial defects and traps are considered as the reason for the failure of the p–n junction. These interfacial trapped charges cause surface $J_{g\text{-}r}$, which results in the leakage current that cannot be suppressed by the reverse bias.

To further determine the interface quality, we tested the response signal of 532 nm light incident from both electrodes. The visible light mainly deposited its energy on the incident surface (~ 500 nm) of the thick film. The distances between the light source and the device surfaces were both 10 cm, to ensure the same incident optical power. As shown in Fig. 5b, when light was incident from ITO, the photocurrent (9.0×10^{-6} A/cm^2 operating at − 20 V) was lower than that from Au (2.5×10^{-5} A/cm^2 at − 20 V). The transmittance of Au layer to 532 nm wavelength light was approximately one-fourth of that of ITO, and the SnO_2 layer was almost completely transparent for 532 nm light (Additional file 1: Fig. S5). Neglecting the light leaking from the edge of the Au electrode, the photo response on $MAPbI_3$ bottom interface was reduced by about 90% at − 20 V. The loss was caused by the nonradiative recombination of interface traps, which demonstrated that the quality of the polycrystalline perovskite thick-film bottom was poor. There is an urgent need for more efficient surface-interface engineering for perovskite thick devices.

Finally, we exposed the X-ray detector with the structure of ITO/SnO_2/$MAPbI_3$/Au to an X-ray source (VARIAN RAD-14) with a 50 kV operation voltage and 25 mA operation current. Attenuated through a 1 mm aluminum plate and a 0.3 mm copper plate, the X-ray beam quality was standard RQA3 and the dose rate was 28.32 μGy_{air}/s. The thickness of the $MAPbI_3$ and SnO_2 film was 438 μm and ~ 100 nm (Additional file 1: Fig. S6) respectively. The current density curve of the thick detector is provided in Fig. 5c. Operating at − 10 V, the light–dark ratio of X-ray response was 14.5 with a stable dark current density of 2.0×10^{-7} A/cm^2. This dark current was on par with the reported performance of $MAPbI_3$ thick-film Schottky device (~ 1.2×10^{-7} A/cm^2 under the same electric field) [48]. As mentioned above, the large dark current was due to the poor quality of the bottom interface resulting in a high $J_{g\text{-}r}$. In addition, there was a lack of a matched electron blocking layer between the perovskite film and the Au electrode to further suppress the current. Figure 5d shows the sensitivities of the thick device versus applied voltages. This X-ray detector exhibited a high sensitivity of 16,300 $\mu C/(Gy_{air}\cdot cm^2)$ at 23 V/cm, which is three orders of magnitude higher than α-Se X-ray detectors (20 $\mu C/(Gy_{air}\cdot cm^2)$), and is high enough for the application of FPXIs [14, 49]. The nonlinear increase of sensitivity with the electric field indicates that the device had high photoelectric gain caused by interfacial and grain boundary defects, which impaired the linear dynamic range of FPXIs. The processing of perovskite thick-film devices needs to be optimized to eliminate this nonlinearity.

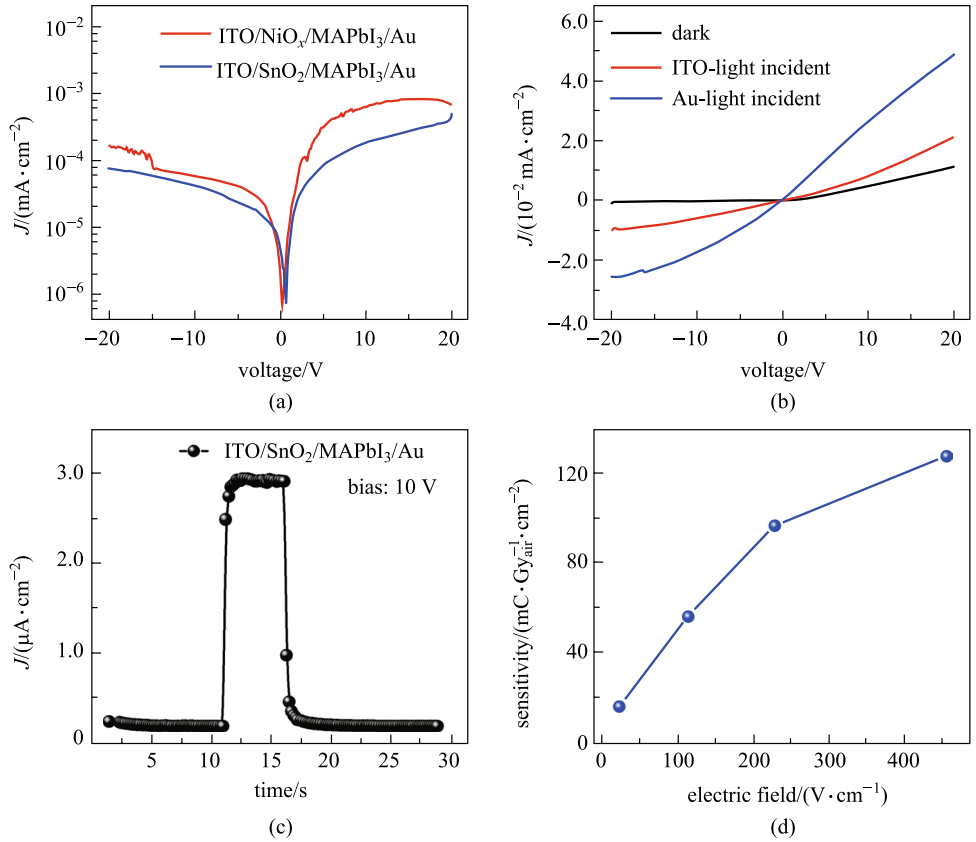

Fig. 5 Detection performance of $MAPbI_3$ thick films. **a** $J-V$ curves of the X-ray detectors with SnO_2 and NiO_x layer. **b** Visible light response-voltage characteristics at both surfaces for the ITO/SnO_2/$MAPbI_3$/Au device. **c** X-ray response, with the electric field set as 238 V/cm. **d** Sensitivity as a function of the electric field

5 Conclusion

In summary, this paper proposes that dark current is an important issue affecting integration of MHP X-ray detectors with pixel circuits. The requirement of dark current is evaluated as 10^{-9} A/cm^2 for FPXIs. To realize this low dark current, it is necessary to redesign the junction device. We reveal the source of the dark current for thick MHP junction detectors as the thermionic-emission current and the generation-recombination current. The former is suppressed by the blocking barrier. The latter is the main reason for the poor performance of thick MHP p–n junctions, which is caused by hetero-band mismatch and interface defects. Due to the interface defect issue, the fabrication of the p–n junction is prone to failure. The related surface-interface engineering and processing need to be intensively studied. Overall, our work provides progress towards optimization of the performance of junction devices for perovskite X-ray detectors applying to FPXIs.

Supplementary Information The online version contains supplementary material available at https://doi.org/10.1007/s12200-022-00044-1.

Acknowledgements This work was supported by the Major State Basic Research Development Program of China (No. 2021YFB3201000), the National Natural Science Foundation of China (Grant Nos. 62074066, 62134003, and 12050005), the Fund for Innovative Research Groups of the Natural Science Foundation of Hubei Province (Nos. 2021CFA036 and 2020CFA034), Shenzhen Basic Research Program (No. JCYJ20200109115212546), and the Fundamental Research Funds for the Central Universities. The authors thank the facility support of the Analytical and Testing Center of HUST. The authors also acknowledge the help from Prof. Chao Chen for the discussion in SCAPS simulation.

Author contributions GN conceived and supervised the whole project. SZ and XYD designed and performed the experiments. JCP and HDW assisted with device optimization and data analysis. SZ and ZHS completed the simulation together. LX and ZPZ helped in the result discussion. SZ and GN wrote the paper and were responsible for the corrections of the manuscript. All authors read and approved the final manuscript.

Declarations

Competing interests The authors have no conflicts to disclose.

References

1. Wei, H., Huang, J.: Halide lead perovskites for ionizing radiation detection. Nat. Commun. **10**(1), 1066 (2019)
2. Dong, Q., Fang, Y., Shao, Y., Mulligan, P., Qiu, J., Cao, L., Huang, J.: Electron-hole diffusion lengths > 175 μm in solution-grown $CH_3NH_3PbI_3$ single crystals. Science **347**, 967–970 (2015)
3. Yin, W., Shi, T., Yan, Y.: Unusual defect physics in $CH_3NH_3PbI_3$ perovskite solar cell absorber. Appl. Phys. Lett. **104**(6), 063903 (2014)
4. Arquer, F., Armin, A., Meredith, P., Sargent, E.H.: Solution-processed semiconductors for next-generation photodetectors. Nat. Rev. Mater. **2**, 16100 (2017)
5. Wei, W., Zhang, Y., Xu, Q., Wei, H., Fang, Y., Wang, Q., Deng, Y., Li, T., Gruverman, A., Cao, L., Huang, J.: Monolithic integration of hybrid perovskite single crystals with heterogenous substrate for highly sensitive X-ray imaging. Nat. Photon. **11**(5), 315–321 (2017)
6. Wang, X., Zhao, D., Qiu, Y., Huang, Y., Wu, Y., Li, G., Huang, Q., Khan, Q., Nathan, A., Lei, W., Chen, J.: PIN diodes array made of perovskite single crystal for X-Ray imaging. Phys. Status Solidi RRL **12**(10), 1800380 (2018)
7. Pan, W., Yang, B., Niu, G., Xue, K., Du, X., Yin, L., Zhang, M., Wu, H., Miao, X., Tang, J.: Hot-pressed $CsPbBr_3$ quasi-monocrystalline film for sensitive direct X-ray detection. Adv. Mater. **31**(44), 1904405 (2019)
8. Huang, Y., Qiao, L., Jiang, Y., He, T., Long, R., Yang, F., Wang, L., Lei, X., Yuan, M., Chen, J.: A-site cation engineering for highly efficient $MAPbI_3$ single-crystal X-ray detector. Angew. Chem. Int. Ed. **58**(49), 17834–17842 (2019)
9. Zhang, Y., Liu, Y., Xu, Z., Ye, H., Yang, Z., You, J., Liu, M., He, Y., Kanatzidis, M.G., Liu, S.: Nucleation-controlled growth of superior lead-free perovskite $Cs_3Bi_2I_9$ single-crystals for high-performance X-ray detection. Nat. Commun. **11**(1), 2304 (2020)
10. Hu, M., Jia, S., Liu, Y., Cui, J., Zhang, Y., Su, H., Cao, S., Mo, L., Chu, D., Zhao, G., Zhao, K., Yang, Z., Liu, S.: Large and dense organic–inorganic hybrid perovskite $CH_3NH_3PbI_3$ wafer fabricated by one-step reactive direct wafer production with high X-ray sensitivity. ACS Appl. Mater. Interfaces **12**(14), 16592–16600 (2020)
11. Peng, J., Xia, C.Q., Xu, Y., Li, R., Cui, L., Clegg, J.K., Herz, L.M., Johnston, M.B., Lin, Q.: Crystallization of $CsPbBr_3$ single crystals in water for X-ray detection. Nat. Commun. **12**(1), 1531 (2021)
12. Wei, H., Fang, Y., Mulligan, P., Chuirazzi, W., Fang, H., Wang, C., Ecker, B.R., Gao, Y., Loi, M.A., Cao, L., Huang, J.: Sensitive X-ray detectors made of methylammonium lead tribromide perovskite single crystals. Nat. Photon. **10**(5), 333–339 (2016)
13. He, Y., Hadar, I., Kanatzidis, M.G.: Detecting ionizing radiation using halide perovskite semiconductors processed through solution and alternative methods. Nat. Photon. **16**(1), 14–26 (2021)
14. Huang, H., Abbaszadeh, S.: Recent developments of amorphous selenium-based X-ray detectors: a review. IEEE Sens. J. **20**(4), 1694–1704 (2020)
15. Szeles, C.: CdZnTe and CdTe materials for X-ray and gamma ray radiation detector applications. Phys. Status Solidi **241**(3), 783–790 (2004)
16. Kasap, S.O., Rowlands, J.A.: Photoconductor selection for digital flat panel X-ray image detectors based on the dark current. J. Vac. Sci. Technol. A **18**(2), 615–620 (2000)
17. Zhao, W., Rowlands, J.A.: X-ray imaging using amorphous selenium: feasibility of a flat panel self-scanned detector for digital radiology. J. Med. Phys. **22**(10), 1595–1604 (1995)
18. Fang, Y., Huang, J.: Resolving weak light of sub-picowatt per square centimeter by hybrid perovskite photodetectors enabled by noise reduction. Adv. Mater. **27**(17), 2804–2810 (2015)
19. Euvrard, J., Yan, Y., Mitzi, D.B.: Electrical doping in halide perovskites. Nat. Rev. Mater. **6**(6), 531–549 (2021)
20. Nayak, P.K., Sendner, M., Wenger, B., Wang, Z., Sharma, K., Ramadan, A.J., Lovrinčić, R., Pucci, A., Madhu, P.K., Snaith, H.J.: Impact of Bi^{3+} heterovalent doping in organic–inorganic metal halide perovskite crystals. J. Am. Chem. Soc. **140**(2), 574–577 (2018)
21. Docampo, P., Ball, J.M., Darwich, M., Eperon, G.E., Snaith, H.J.: Efficient organometal trihalide perovskite planar-heterojunction solar cells on flexible polymer substrates. Nat. Commun. **4**(1), 2761 (2013)
22. Tan, Z., Moghaddam, R.S., Lai, M.L., Docampo, P., Higler, R., Deschler, F., Price, M., Sadhanala, A., Pazos, L.M., Credgington, D., Hanusch, F., Bein, T., Snaith, H.J., Friend, R.H.: right light-emitting diodes based on organometal halide perovskite. Nat. Nanotechnol. **9**(9), 687–692 (2014)
23. Dou, L., Yang, Y., You, J., Hong, Z., Chang, W., Li, G., Yang, Y.: Solution-processed hybrid perovskite photodetectors with high detectivity. Nat. Commun. **5**(1), 5404 (2014)
24. Stranks, S.D., Snaith, H.J.: Metal-halide perovskites for photovoltaic and light-emitting devices. Nat. Nanotechnol. **10**(5), 391–402 (2015)
25. He, Y., Ke, W., Alexander, G.C.B., McCall, K.M., Chica, D.G., Liu, Z., Hadar, I., Stoumpos, C.C., Wessels, B.W., Kanatzidis, M.G.: Resolving the energy of γ-ray photons with $MAPbI_3$ single crystals. ACS Photonics **5**(10), 4132–4138 (2018)
26. He, Y., Matei, L., Jung, H.J., McCall, K.M., Chen, M., Stoumpos, C.C., Liu, Z., Peters, J.A., Chung, D.Y., Wessels, B.W., Wasielewski, M.R., Dravid, V.P., Burger, A., Kanatzidis, M.G.: High spectral resolution of gamma-rays at room temperature by perovskite $CsPbBr_3$ single crystals. Nat. Commun. **9**(1), 1609 (2018)
27. He, Y., Petryk, M., Liu, Z., Chica, D.G., Hadar, I., Leak, C., Ke, W., Spanopoulos, I., Lin, W., Chung, D.Y., Wessels, B.W., He, Z., Kanatzidis, M.G.: $CsPbBr_3$ perovskite detectors with 1.4% energy resolution for high-energy γ-rays. Nat. Photon. **15**(1), 36–42 (2021)
28. Peng, J., Ye, K., Xu, Y., Cui, L., Li, R., Peng, H., Lin, Q.: X-ray detection based on crushed perovskite crystal/polymer composites. Composites Sens. Actuators A **312**, 112132 (2020)
29. Wei, H., DeSantis, D., Wei, W., Deng, Y., Guo, D., Savenije, T.J., Cao, L., Huang, J.: Dopant compensation in alloyed $CH_3NH_3PbBr_{3-x}Cl_x$ perovskite single crystals for gamma-ray spectroscopy. Nat. Mater. **16**(8), 826–833 (2017)
30. Kim, Y.C., Kim, K.H., Son, D., Jeong, D., Seo, J., Choi, Y.S., Han, I.T., Lee, S.Y., Park, N.: Printable organometallic perovskite enables large-area, low-dose X-ray imaging. Nature **550**(7674), 87–91 (2017)
31. Zhou, Y., Zhao, L., Ni, Z., Zhao, J., Xiao, X., Huang, J.: Heterojunction structures for reduced noise in large-area and sensitive perovskite X-ray detectors. Sci. Adv. **7**(36), 6716 (2021)

32. Xu, Y., Jiao, B., Song, T., Stoumpos, C.C., He, Y., Hadar, I., Lin, W., Jie, W., Kanatzidis, M.G.: Zero-dimensional Cs_2TeI_6 perovskite: solution-processed thick films with high X-ray sensitivity. ACS Photonics **6**(1), 196–203 (2018)
33. Thompson, M., Ellison, S.L.R., Wood, R.: Harmonized guidelines for single-laboratory validation of methods of analysis (IUPAC Technical Report). Pure Appl. Chem. **74**(5), 835–855 (2002)
34. El-Gabaly, M., Nigrin, J., Goud, P.A.: Stationary charge transport in metal-semiconductor-metal (MSM) structures. J. Appl. Phys. **44**(10), 4672–4680 (1973)
35. Sze, S.M., Ng, K.K.: Physics of semiconductor devices, 3rd ed. Hoboken: John Wiley & Sons, 80-88, 166–169 (2006)
36. Homes, C.C., Vogt, T., Shapiro, S.M., Wakimoto, S., Ramirez, A.P.: Optical response of high-dielectric-constant perovskite-related oxide. Science **293**(5530), 673–676 (2001)
37. Ni, Z., Bao, C., Liu, Y., Jiang, Q., Wu, W., Chen, S., Dai, X., Chen, B., Hartweg, B., Yu, Z., Holman, Z., Huang, J.: Resolving spatial and energetic distributions of trap states in metal halide perovskite solar cells. Science **367**(6484), 1352–1358 (2020)
38. Wu, C.Y.: Interfacial layer-thermionic-diffusion theory for the Schottky barrier diode. J. Appl. Phys. **53**(8), 5947–5950 (1982)
39. Colinge, J.P., Colinge, C.A.: Physics of semiconductor devices. Springer Science & Business Media, Berlin (2005)
40. Ollearo, R., Wang, J., Dyson, M.J., Weijtens, C.H.L., Fattori, M., van Gorkom, B.T., van Breemen, A.J.J.M., Meskers, S.C.J., Janssen, R.A.J., Gelinck, G.H.: Ultralow dark current in near-infrared perovskite photodiodes by reducing charge injection and interfacial charge generation. Nat. Commun. **12**(1), 7277 (2021)
41. Jiang, Q., Zhang, X., You, J.: SnO_2: a wonderful electron transport layer for perovskite solar cells. Small **14**(31), 1801154 (2018)
42. Baikie, T., Fang, Y., Kadro, J.M., Schreyer, M., Wei, F., Mhaisalkar, S.G., Graetzel, M., White, T.J.: Synthesis and crystal chemistry of the hybrid perovskite $(CH_3NH_3)PbI_3$ for solid-state sensitised solar cell applications. J. Mater. Chem. A **1**(18), 5628–5641 (2013)
43. Raoui, Y., Ez-Zahraouy, H., Tahiri, N., Bounagui, O.E., Ahmad, S., Kazim, S.: Performance analysis of $MAPbI_3$ based perovskite solar cells employing diverse charge selective contacts: Simulation study. Sol. Energy **193**, 948–955 (2019)
44. Wehrenfennig, C., Eperon, G.E., Johnston, M.B., Snaith, H.J., Herz, L.M.: High charge carrier mobilities and lifetimes in organolead trihalide perovskites. Adv. Mater. **26**(10), 1584–1589 (2014)
45. Shukl, V., Panda, G.: The performance study of CdTe/CdS/SnO_2 solar cell. Mater. Today Proc. **26**, 487–491 (2020)
46. Xia, M., Song, Z., Wu, H., Du, X., He, X., Pang, J., Luo, H., Jin, L., Li, G., Niu, G., Tang, J.: Compact and large-area perovskite films achieved via soft-pressing and multi-functional polymerizable binder for flat-panel X-ray imager. Adv. Funct. Mater. **32**(16), 2110729 (2022)
47. Bansal, S., Aryal, P.: Evaluation of new materials for electron and hole transport layers in perovskite-based solar cells through SCAPS-1D simulations. 2016 IEEE 43rd Photovoltaic Specialists Conference (PVSC), 0747–0750 (2016)
48. Deumel, S., van Breemen, A., Gelinck, G., Peeters, B., Maas, J., Verbeek, R., Shanmugam, S., Akkerman, H., Meulenkamp, E., Huerdler, J.E., Acharya, M., Batlle, M.G., Almora, O., Guerrero, A., Belmonte, G.G., Heiss, W., Schmidt, O., Tedde, S.F.: High-sensitivity high-resolution X-ray imaging with soft-sintered metal halide perovskites. Nat. Electron. **4**(9), 681–688 (2021)
49. Hunter, D.M., Belev, G., Kasap, S., Yaffe, M.J.: Measured and calculated K-fluorescence effects on the MTF of an amorphous-selenium based CCD X-ray detector. Med. Phys. **39**, 608–622 (2012)

Shan Zhao received her Bachelor's degree in Electronic Science and Technology from Huazhong University of Science and Technology, China in 2020, and she is currently a Master candidate in Wuhan National Laboratory for Optoelectronics, Huazhong University of Science and Technology. She is engaged in research on perovskite high-energy radiation detectors.

Xinyuan Du received his Bachelor's degree in Optical Engineering from Huazhong University of Science and Technology, China in 2018, and he is currently a Ph.D. candidate in Wuhan National Laboratory for Optoelectronics, Huazhong University of Science and Technology. He is engaged in research on perovskite X-ray detectors.

Jincong Pang received his Bachelor's degree in Optical Engineering from Huazhong University of Science and Technology, China in 2019, and he is currently a Ph.D. candidate in Wuhan National Laboratory for Optoelectronics, Huazhong University of Science and Technology. He is engaged in research on single crystals for radiation detectors.

Haodi Wu received his Bachelor's degree in Optoelectronic Information Science and Engineering from Jilin University, China in 2016, and Ph.D. degree in Optical Engineering from Wuhan National Laboratory for Optoelectronics, Huazhong University of Science and Technology, China in 2021. He spent one year as a postdoctoral researcher at Wuhan National Laboratory for Optoelectronics in 2022. He is engaged in research on high-energy radiation detectors.

Zihao Song received his Bachelor's degree in Material Physics from Jilin University, China in 2020, and he is currently a Ph.D. candidate in Wuhan National Laboratory for Optoelectronics, Huazhong University of Science and Technology, China. He is engaged in research on perovskite X-ray detectors.

Zhiping Zheng received her M.S. and Ph.D. degrees from Huazhong University of Science and Technology, China in 2002 and 2005, respectively, both in Electronic Science and Technology. She joined School of Optical and Electronic Information, Huazhong University of Science and Technology, China as a lecturer. Now she is a professor. She is engaged in research on semiconductor single crystals, functional ceramics and detectors.

Ling Xu received his Ph.D. degree in Material Physics and Chemistry from Huazhong University of Science and Technology, China in 2010. From November 2010, he joined Wuhan National Laboratory for Optoelectronics, China. In December 2015, he was promoted to an Associate Professor. He is engaged in research on photoelectric materials and devices.

Jiang Tang received his Bachelor's degree from University of Science and Technology, China in 2003, and Ph.D. degree in Material Science and Engineering from University of Toronto, Canada in 2010. He spent one year and half as a postdoctoral researcher at IBM T. J. Watson Research Center and then joined Wuhan National Laboratory for Optoelectronics, Huazhong University of Science and Technology, China as a professor in 2012. His group focuses on antimony selenide (Sb_2Se_3) thin film solar cells, halide perovskites nanocrystals for light emitting and single crystals for X-ray detection. He has published 150+ papers on prestigious magazines, including Nature, Nature Materials, Nature Energy, and Nature Photonics.

Guangda Niu received his Bachelor's degree from Nanjing University, China in 2011 and his Ph.D. degree from Tsinghua University, China in 2016. He is engaged in research on halide perovskite based radiation detectors.